AIAA JOURNAL
Vol. 39, No. 11, November 2001

Discontinuous Spectral Element Solution of Acoustic Radiation from Thin Airfoils

Patrick Rasetarinera,* David A. Kopriva,† and M. Y. Hussaini†
Florida State University, Tallahassee, Florida 32306

A time-domain spectral element method is used to compute the acoustic radiation from thin airfoils generated in response to upstream, small amplitude plane vorticity waves. The method is a spectral element (collocation) form of the discontinuous Galerkin method for the solution of the Euler gasdynamics equations. Solutions are presented for flat plate and symmetric and nonsymmetric Joukowski airfoils. Comparisons are made to semi-analytic and finite difference computations.

Nomenclature

$\boldsymbol{a}$	=	vortical gust amplitude vector, (a_1, a_2)
c	=	chord length
e	=	specific total energy
F, G	=	inviscid Euler fluxes
J	=	Jacobian
$\boldsymbol{k}$	=	wave number vector normalized by $2/c$, (k_1, k_2)
ℓ	=	Lagrange interpolating polynomial
M	=	Mach number
p	=	pressure normalized by $\rho_\infty U_\infty^2$
p_{ss}	=	steady-state pressure normalized by $\rho_\infty U_\infty^2$
p'	=	perturbation pressure normalized by $\rho_\infty U_\infty^2$
$\boldsymbol{Q}$	=	vector of dependent variables
S	=	source term
t	=	time normalized by $c/(2U_\infty)$
U_∞	=	upstream mean velocity
u, v	=	Cartesian velocity components normalized by U_∞
$\boldsymbol{x}$	=	Cartesian coordinates normalized by $c/2$, (x, y)
γ	=	specific heat ratio
Δ_x, Δ_y	=	mesh size in the x and y directions
θ	=	angle with respect to x axis
ξ, η	=	local coordinates in the unit square
ρ	=	density normalized by ρ_∞

Subscript

∞	=	freestream quantity

I. Introduction

WHEN aircraft components such as wings or turbomachinery blades interact with freestream vorticity that is characteristic of turbulent or rotating flows, sound is generated. The effectiveness of finite difference time-domain methods to predict such sound has been the subject of study in recent papers. Hariharan et al.[1] solved the convective wave equation with a second-order finite difference method for the sound generated by a flat plate. The flat plate problem was revisited by Grace et al.,[2] who used a second-order finite difference method and the linearized Euler equations to compute the sound. A high-order finite difference method was used by Lockard and Morris[3] to solve the flat plate problem and a finite thickness airfoil.[4] Recently, Hariharan et al.[5] computed the sound generated by both lifting and nonlifting airfoils.

The difficulties in computing the sound generated in an airfoil/gust interaction are addressed in Refs. 1 and 2. Many of the difficulties arise from the multiple scales involved. Among the spatial scales are the airfoil chord length, the length scale associated with the steady perturbation of the airfoil on the mean flow, the wavelength of the incident vorticity, and the scale on which the solution is desired. The incident vorticity and generated sound waves must be accurately computed in the far field, which means that typical steady-state computational fluid dynamics (CFD) meshes are not appropriate.[3] Imposition of the external boundary conditions, with the need to impose the vorticity wave on a nonuniform mean flow while allowing for the radiation of the generated sound is another source of difficulty.

We propose to address the multiple-scale issues associated with the airfoil/gust problem by using a discontinuous spectral element method (DSEM). Spectral element methods in general are high order, flexible extensions of the spectral collocation method.[6] Like finite volume or finite element methods, complex geometries are subdivided into multiple elements. Within each element, the solution is approximated by an orthogonal polynomial expansion. Local resolution of the solution can be increased either by decreasing the size of the elements or by increasing the order of the polynomials. The particular method used here is a high-order spectral element version of the discontinuous Galerkin method (see Ref. 7).

For the airfoil/gust interaction problems, DSEMs have practical advantages over high-order finite difference methods. They are designed to handle complex geometries and can use unstructured element grids generated by commercial mesh generation codes.[8] Though block-structured finite difference methods permit solutions in complex geometries, DSEMs are not restricted to meshes with smooth metrics. Also, DSEMs approximate boundary surfaces to the same high order as the solution is approximated. Cartesian mesh finite difference methods, for instance, do not.

Unlike high-order finite difference methods, spectral element methods are compact. Their stencil resides completely within an element, independent of the approximation order. This means that there are no ghost point issues to complicate the approximation and implementation of boundary conditions. Also, elements can be sized according to the needs of the solution without regard to the size of neighboring elements. This gives complete flexibility for changing element sizes, unlike high-order finite difference methods for which changes in mesh sizes by factors of two are most convenient.[9]

Spectral element methods are robust. Unlike centered finite difference methods, they do not require the addition of specially tuned artificial dissipation, compare Ref. 3. Also, the discontinuous spectral element method described here does not require special treatment of corner points. This means that special programming is not needed for complex grid topologies or for sharp edges.

Finally, spectral element methods have spectrally small phase and dissipation errors. Waves can propagate over a large number of wavelengths with a minimal number of points per wavelength while keeping the flexibility described earlier. Examples can be found in Refs. 10–12. An analysis of the phase and dissipation errors of the

Received 8 November 2000; revision received 9 May 2001; accepted for publication 10 May 2001.

*Postdoctoral Research Associate, School of Computational Science and Information Technology, 400 Dirac Science Library.

†Professor, School of Computational Science and Information Technology, 400 Dirac Science Library.

discontinuous Galerkin method has also been performed recently and is described in Refs. 12–14. In the first of these, it was shown that for simple advection problems and polynomial orders of six–eight, only five–six points per wavelength are needed. If one uses polynomial orders between 8 and 16, only four–five points per wavelength are needed.

In this paper we present solutions to three problems. The first is the noise radiated by a flat plate in response to a plane vorticity wave. The solutions for this problem are compared to analytic solutions. The second problem is the response of a nonlifting finite thickness airfoil. Finally, we present results for the noise generated by a lifting airfoil.

II. Solution Approach

A. Equations

We approximate the two-dimensional, nonlinear compressible Euler equations of gasdynamics in conservative form:

$$Q_t + \nabla \cdot \boldsymbol{F} = Q_t + F_x + G_y = S \tag{1}$$

Explicitly, we have

$$Q = \begin{bmatrix} \rho \\ \rho u \\ \rho v \\ \rho e \end{bmatrix}, \qquad F = \begin{bmatrix} \rho u \\ p + \rho u^2 \\ \rho uv \\ u(\rho e + p) \end{bmatrix}, \qquad G = \begin{bmatrix} \rho v \\ \rho uv \\ p + \rho v^2 \\ v(\rho e + p) \end{bmatrix}$$

We assume an ideal gas with $\rho e = p/(\gamma - 1) + (u^2 + v^2)/2$ and $\gamma = 1.4$. The quantity S on the right-hand side of Eq. (1) represents a source term.

B. Discontinuous Galerkin Spectral Element Method

In two space dimensions, the region under consideration is divided into nonoverlapping elements. The elements can have a general quadrilateral shape to permit the accurate resolution of curved boundaries with a minimum number of elements. Each element is mapped individually onto the unit square by an isoparametric transformation (e.g., see Ref. 15).

On each element, the mapping transforms Eq. (1) to

$$\tilde{Q}_t + \nabla_\xi \cdot \tilde{\boldsymbol{F}} = \tilde{Q}_t + \tilde{F}_\xi + \tilde{G}_\eta = \tilde{S} \tag{2}$$

The new variables are $\tilde{Q} = JQ$, $\tilde{S} = JS$, and

$$\tilde{F} = y_\eta F - x_\eta G, \qquad \tilde{G} = -y_\xi F + x_\xi G$$

$$J(\xi, \eta) = x_\xi y_\eta - x_\eta y_\xi \tag{3}$$

The discontinuous Galerkin version of the spectral element method approximates the solution and the fluxes by the Nth-order polynomials

$$\tilde{\boldsymbol{Q}}(\xi, \eta) = \sum_{\mu,\nu=0}^{N} \tilde{\boldsymbol{Q}}_{\mu,\nu} \phi_{\mu,\nu}, \qquad \tilde{\boldsymbol{F}}(\xi, \eta) = \sum_{\mu,\nu=0}^{N} \tilde{\boldsymbol{F}}_{\mu,\nu} \phi_{\mu,\nu} \tag{4}$$

where $\phi_{\mu,\nu} = \ell_\mu(\xi)\ell_\nu(\eta)$. The Lagrange interpolating polynomials ℓ_i are defined at the Legendre–Gauss quadrature points. The nodal values of the flux are computed from the nodal values of the solution, that is, $\tilde{\boldsymbol{F}}_{i,j} = \tilde{\boldsymbol{F}}(\tilde{\boldsymbol{Q}}_{i,j})$. No assumptions are made about the continuity of the solution, $\tilde{\boldsymbol{Q}}$, across element boundaries.

In this approximation, the residual is required to be orthogonal to the approximation space within an element, so that

$$(\tilde{\boldsymbol{Q}}_t, \phi_{i,j}) + (\nabla_\xi \cdot \tilde{\boldsymbol{F}}, \phi_{i,j}) = (\tilde{\boldsymbol{S}}, \phi_{i,j}), \qquad i, j = 0, 1, \ldots, N \tag{5}$$

where $(\cdot, \cdot)$ represents the usual L^2 inner product.

Integration of Eq. (5) by parts gives

$$(\tilde{\boldsymbol{Q}}_t, \phi_{i,j}) + \int_{\partial E} \phi_{i,j} \tilde{\boldsymbol{F}} \cdot \hat{N}\, \mathrm{d}S - (\tilde{\boldsymbol{F}}, \nabla_\xi \phi_{i,j}) = (\tilde{\boldsymbol{S}}, \phi_{i,j})$$

$$i, j = 0, 1, \ldots, N \tag{6}$$

where ∂E represents the boundary of the element.

To obtain equations for the nodal values of the solution, $\tilde{\boldsymbol{Q}}_{i,j}$, the integrals in Eq. (6) are replaced by Legendre–Gauss quadratures, which have the property that

$$\int_{-1}^{1} v(\xi, \eta)\, \mathrm{d}\xi\, \mathrm{d}\eta = \sum_{i,j=0}^{N} v(\xi_i, \eta_j) w_i w_j \tag{7}$$

for all polynomials v that are of degree $2N + 1$ or less. The replacement is exact provided that the element sides are straight. If the sides are curved, however, an additional quadrature error is incurred, just as in the spectral element method for parabolic equations.[16] The advantage gained by using quadrature is that the mass matrix generated by $(\tilde{\boldsymbol{Q}}_t, \phi_{i,j})$ remains diagonal and trivially invertible. This makes the use of high-order elements practical and efficient for wave-propagation problems.

After some manipulation, the final approximation in two space dimensions is

$$\frac{\mathrm{d}\tilde{Q}_{i,j}}{\mathrm{d}t} + \left[\tilde{F}(1, \eta_j) \frac{\ell_i(1)}{w_i} - \tilde{F}(0, \eta_j) \frac{\ell_i(0)}{w_i} - \sum_\mu \tilde{F}_{\mu,j} \frac{(\ell_i', \ell_\mu)_N}{w_i} \right]$$

$$+ \left[\tilde{G}(\xi_i, 1) \frac{\ell_j(1)}{w_j} - \tilde{G}(\xi_i, 0) \frac{\ell_j(0)}{w_j} \right.$$

$$\left. - \sum_\mu \tilde{G}_{\mu,j} \frac{(\ell_j', \ell_\mu)_N}{w_j} \right] = \tilde{S}_{i,j} \tag{8}$$

where the discrete inner product is the Gauss quadrature

$$(u, v)_N = \sum_{i=0}^{N} u_i v_i w_i \tag{9}$$

Note that, if the approximating polynomial order is zero, Eq. (8) reduces to a first-order finite volume method.

The flux quantities $F(0, \eta_j)$, $F(1, \eta_j)$, $G(\xi_i, 1)$, and $G(\xi_i, 0)$ in Eq. (8) represent the element boundary fluxes. As in a finite volume approximation, the solutions are discontinuous at element faces. A Riemann solver is used to compute a continuous flux at the element faces from the discontinuous solution values. For the nonlinear computations presented here, we have used Roe's[17] approximate Riemann solver.

To increase the flexibility of the method by allowing the adjustment of the approximating polynomials locally, we allow nonconforming approximations. The procedure for computing the boundary fluxes when the polynomial orders do not match is described in Ref. 18.

The semidiscrete approximation [Eq. (8)] is integrated in time by a low-storage Runge–Kutta method. Both third- and fourth-order methods are used (compare Ref. 15).

C. Boundary Conditions

The use of the Riemann solver at element faces makes the imposition of boundary conditions simple. Boundary conditions are implemented by specifying the external state as the input for the Riemann solver (see Ref. 15).

In multidimensional problems, it is also necessary to implement radiation boundary conditions. In this paper, we treat the outgoing pressure waves through a damping-layer procedure, which is easy to apply and inexpensive. Coupled with the characteristic boundary conditions implicit in the use of the Riemann solver at the exterior boundary, the damping-layer approach is effective; compare Ref. 19. Our damping-layer approach sets the source term on the right of Eq. (1) so that sound waves are damped in time as they propagate toward the outer boundaries. Only the radiating sound waves are damped, so that the damping term is written as

$$S = \frac{\sigma}{\gamma - 1} \begin{bmatrix} 0 \\ 0 \\ 0 \\ p - p_{ss} \end{bmatrix} \tag{10}$$

where p_{ss} is the steady-state pressure. The quantity σ is a ramp function that grows smoothly from zero as the outer boundary is approached. We use two such ramp functions. The first increases the damping radially as

$$\sigma(r) = \beta\left(\frac{r - r_0}{r_{\max} - r_0}\right)^{\nu} \tag{11}$$

where r is the radial direction, measured from the center of the airfoil. The rate at which the ramp function increases, ν, was chosen to be either one or two. A second ramp function replaced the radial direction with the boundary-normal direction within an element along the outer boundary. Using two different ramp functions and varying r_0 and $r_{\max}$ permitted us to assess any contamination of the solution by spurious reflected sound waves.

D. Steady-State Computation

Like the computations presented in Ref. 3, the steady solutions of the finite thickness airfoils are computed first. Once a steady solution is found, the incident waves are imposed as boundary conditions. This splitting permits the use of convergence acceleration techniques to get the steady state. Here we use local time stepping.[8] We estimate that, on the finite thickness airfoil problems with fixed polynomial order, the computation of the steady state is accelerated by a factor of 30 using local time stepping. All steady-state flow solutions were converged to double precision machine accuracy, with residuals on the order of 10^{-12}.

III. Solutions

We now compute the unsteady aerodynamic and aeroacoustic response of a single airfoil to a two-dimensional, periodic vortical gust. In this problem, an incident gust

$$\boldsymbol{U} = U_\infty \boldsymbol{i} + \boldsymbol{a}\cos[\boldsymbol{k}\cdot(\boldsymbol{x} - \boldsymbol{i}U_\infty t)] \tag{12}$$

where $\boldsymbol{a} = (-\epsilon U_\infty k_2/|\boldsymbol{k}|, \epsilon U_\infty k_1/|\boldsymbol{k}|)$ is the amplitude of the vortical disturbance with $\epsilon = 0.02$ that propagates from infinity with the mean flow toward the airfoil. At the airfoil surface, sound and vorticity are generated. The sound propagates outward in all directions from the airfoil, while the vorticity propagates as a vortex street off the trailing edge of the airfoil. We solve this problem in the total-field formulation: We impose the gust as an external boundary condition and compute the periodic solution as the time-asymptotic solution of the Euler equations.

Three airfoil shapes are considered. The first is a flat plate with chord length two. The second and third are Joukowski airfoils. The Joukowski airfoils are generated by setting

$$\zeta_1 = r_0 e^{i\theta} + \zeta_{0'} \tag{13}$$

where

$$\zeta_{0'} = -\varepsilon_1 + i\varepsilon_2 \tag{14}$$

With the usual definition of the complex variable $z = x + iy$, the airfoil coordinates are given by

$$z = \left(\zeta_1 + d^2/\zeta_1\right)e^{-i\alpha} \tag{15}$$

For the nonlifting case (Sec. III.B), $r_0 = 0.54632753$, $\varepsilon_1 = 0.05062004$, $\varepsilon_2 = 0.0$, $d^2 = 0.24572591$, and $\alpha = 0.0$. The lifting case (Sec. III.C) uses $r_0 = 0.54676443$, $\varepsilon_1 = 0.05062004$, $\varepsilon_2 = 0.02185310$, $d^2 = 0.24572591$, and $\alpha = 0.034906585$.

Two important computational issues are the choice of mesh topology and the size of the mesh. The mean flow must be well resolved in the neighborhood of the airfoil. Unlike a pure CFD calculation, however, it is also necessary to have uniform resolution in the far field with which to represent the incoming gust, the expanding sound wave, and the vorticity advected downstream from the airfoil. These needs indicate that a grid formed by a conformal mapping would not be efficient because the conformal grid will produce large elements in the far field. For this reason, we use unstructured grids. Figures 1 and 2 show representative examples of meshes used about the airfoils.

For the finite thickness airfoils, the distance of the external boundaries from the airfoil also affects the solution. As in a CFD calculation, the outer boundary must be far enough away so that the surface pressure is not affected by the boundary placement. An additional constraint is that the velocity in the external regions must be close enough to the uniform freestream value so that the assumption of setting the gust at the outer boundary as a plane wave is accurate. For instance, we find that the mean flow velocity is within 2.5% of the freestream velocity at about 7.5 chord lengths from the nonlifting airfoil of Sec. III.B. For the lifting case described in Sec. III.C, on the other hand, it is necessary to extend the mesh to 22.5 chord lengths in each direction to get a solution independent of the outer mesh distance.

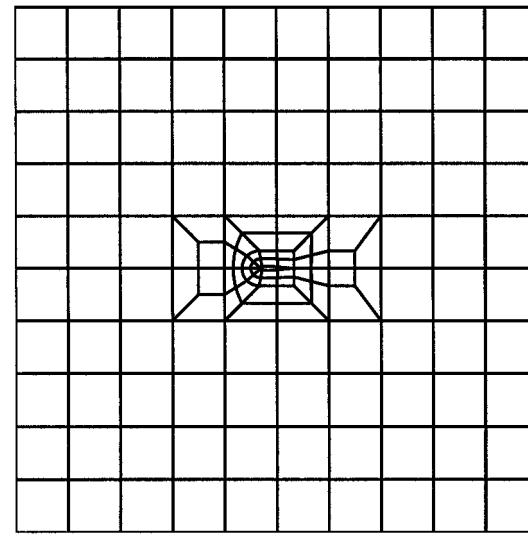

Fig. 1 Mesh topology for the nonlifting airfoil.

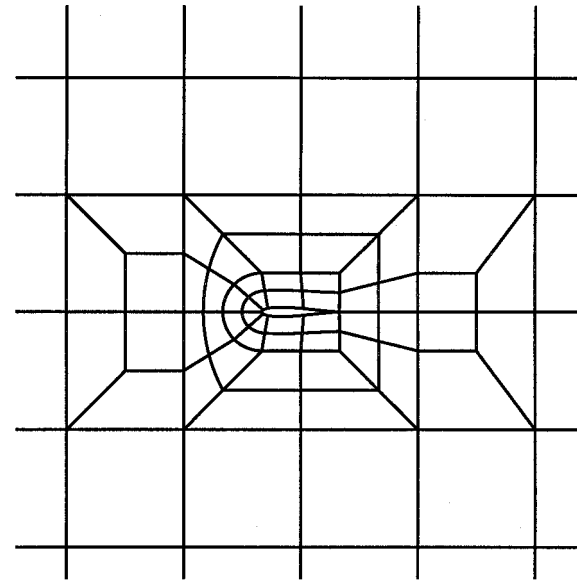

Fig. 2 Closeup of a mesh in the neighborhood of the airfoil.

Two independently written DSEM codes were used to compute the solutions presented here. Code 1 uses elements with straight sides except on the airfoil surfaces. It parameterizes the airfoil surfaces by polar angle θ, which gives better resolution in the neighborhood of the trailing edge. The damping layer in code 1 has a ramping function that grows in the element normal direction. Code 2 has the ability to use curved element boundaries on all elements, as shown in Fig. 2. It parameterizes the airfoil surfaces by arc length except near the leading edge, where polar angle θ is used. The damping layer in code 2 is circular, as described in Eq. (11). Both codes permit the use of variable-order meshes so that the order of the approximating polynomials can be adjusted locally to provide the desired resolution. The use of the two codes permitted the assessment of the effects of the radiation boundary conditions, resolution along the airfoil surface, and element shape.

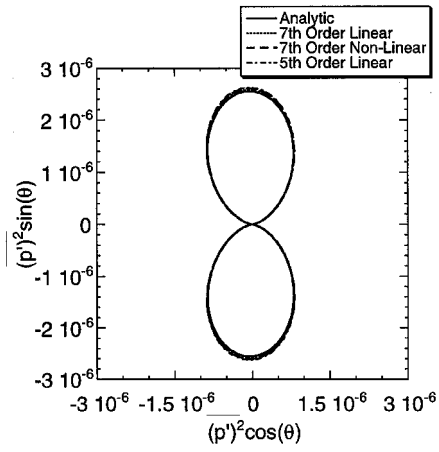

Fig. 3 Acoustic intensity at radius eight for the flat plate and for gust wave number $k_1 = k_2 = 1$.

A. Acoustic Response of a Flat Plate

The first problem that we consider is the unsteady aeroacoustic response of the vortical gust on a flat plate. We compare linear and nonlinear numerical solutions from the DSEM to semi-analytical reference solutions.[20]

To compute the unsteady aeroacoustic response of the vortical gust, we discretize both the linearized Euler equations and the full nonlinear Euler equations in a rectangular domain on a uniform mesh. The initial condition is set to the normalized freestream conditions, and Eq. (12) for the vortical gust is enforced at the boundaries of the domain.

In the computations presented here, the freestream Mach number is set to $M_\infty = 0.5$. The numerical solutions are computed in a rectangular domain $[-31, 31] \times [-30, 30]$ with uniformly sized elements with $\Delta_x = \Delta_y = 2$. In the computational domain, the infinitely thin airfoil lies between $x = -1$ and 1 and is represented by an interface between two elements where a free-slip wall boundary condition is specified on both sides of the interface.

The acoustic responses are computed for two wavelengths. The longer wavelength, with $k_1 = k_2 = 1$, is approximately 2.25 chord lengths. The shorter, with $k_1 = k_2 = 3$, is approximately 1.5 chord lengths.

A rectangular damping layer that extends approximately three wavelengths is used to absorb the outgoing acoustic waves. The parameter for the ramp function (11) is set to $\beta = 1.5$ for $k_1 = k_2 = 1$ and $\beta = 3.0$ for $k_1 = k_2 = 3$. In both cases, $\nu = 2$.

Figure 3 compares computed acoustic intensities $\overline{(p')^2}$ with a semi-analytical solution at a radius of 4.0 chord lengths from the plate for $k_1 = k_2 = 1$. Included are a linear and a nonlinear calculation using seventh-order polynomials in each element plus a linear calculation using fifth-order polynomials. The fifth-order solution corresponds to a resolution of the incident wave of approximately 18 points per wavelength, whereas the seventh-order approximation corresponds to 25. We can see that the linear solution at both resolutions follows the reference solution closely, with a maximum deviation of about 1% for the seventh-order solution. From the nonlinear solution, we see that nonlinear effects are negligible.

Figure 4 compares computed acoustic intensities with the semi-analytical solution at a radius of 4.0 chord lengths from the plate for the higher frequency with $k_1 = k_2 = 3$. The calculation used a polynomial order of seven, which corresponds to approximately seven points per wavelength for the incident wave. Again, we see that the linear solution follows the reference solution closely, with a maximum deviation this time of about 2%.

B. Nonlifting Airfoil Solutions

The steady pressure on the surface of the symmetric airfoil is shown in Fig. 5. The grid used for these calculations extended 7.5 cord lengths from the airfoil. The fixed-order computation used 11th-order polynomials in all elements. The variable-order computations used polynomial orders between 6 and 11, arranged to approximate a uniform eight points per wavelength of the incident gust.

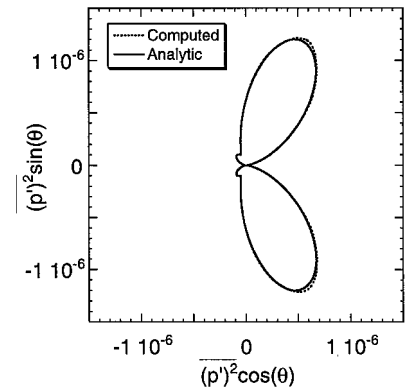

Fig. 4 Acoustic intensity at radius eight for the flat plate and for gust wave number $k_1 = k_2 = 3$.

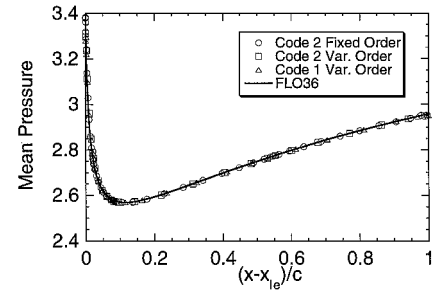

Fig. 5 Steady surface pressure for the symmetric airfoil as a function of distance along the horizontal, scaled to the chord length.

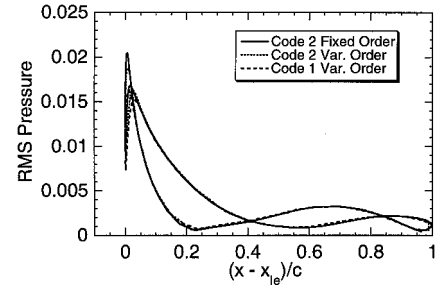

Fig. 6 Symmetric airfoil and gust wave number $k_1 = k_2 = 3$ rms surface pressure.

The fixed-order calculation put 95 points along the airfoil surface. For the variable-order cases, the code 1 solution used 59 points, and the code 2 solution put 55 points along the surface. The computed solutions are compared to a FLO36 solution.[21] Note particularly that the DSEMs have no problem approximating the solution near the sharp trailing edge of the airfoil.

We first show solutions to the nonlifting airfoil for wave number $k_1 = k_2 = 3$. The acoustic response along the surface is shown in Fig. 6. We find that the three solutions are consistent with each other except at the leading edge. There, the peak pressure is sensitive to the resolution. In particular, the three curves show that the lower the resolution is, the lower the peak amplitude.

The computed acoustic intensity is shown in Fig. 7. Shown are the solutions corresponding to the three solutions in Figs. 5 and 6 plus an additional solution computed on a mesh that extended 11.5 chord lengths in each direction. The damping layer in the larger calculation extended three wavelengths beyond the others. The directivity patterns indicate that the radiation boundary conditions are not significantly affecting the solutions. The small difference in the peak values, with variation of 7% or less, can be attributed to the difference in the peak values at the leading edge of the airfoil.

Figures 5–7 show that the solutions, computed with different codes and different meshes, give consistent results. Note, however, that the different computational costs between using the variable-order and the fixed-order meshes. For instance, code 2 required

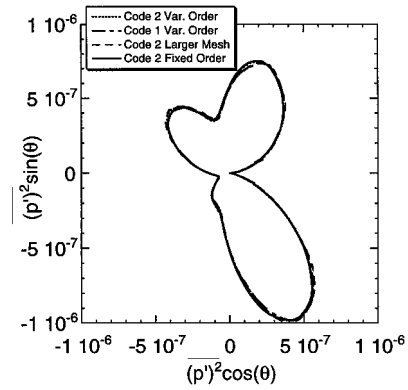

Fig. 7 Acoustic intensity at radius eight for the symmetric airfoil and for gust wave number $k_1 = k_2 = 3$.

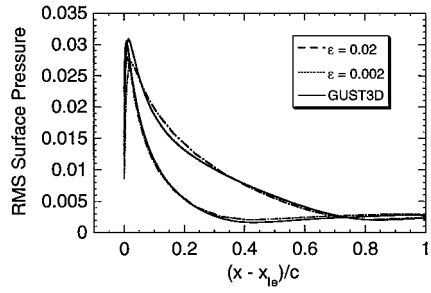

Fig. 8 Symmetric airfoil with gust wave number $k_1 = k_2 = 1$ rms surface pressure; solutions for the gust amplitude $\epsilon = 0.02$ and 0.002 scaled by 100.

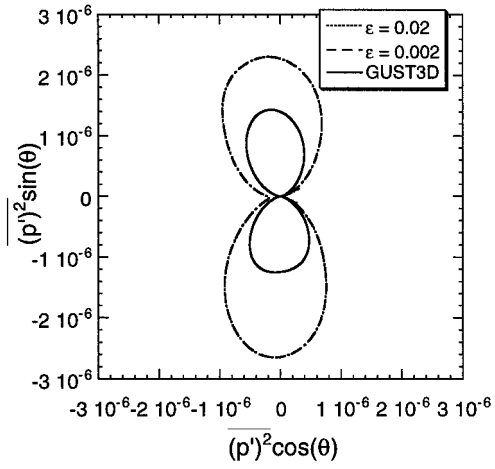

Fig. 9 Acoustic intensity at radius eight for the symmetric airfoil with gust wave number $k_1 = k_2 = 1$; solutions shown for the gust amplitude $\epsilon = 0.02$ and 0.002 scaled by 100; reference solution shown for comparison.

6.4 h on a single processor of an SGI Origin 200 computer to compute both the steady and time-dependent parts of the solution using the variable-order mesh. The fixed-order solution required 19 h. The factor of three difference between the two can be attributed to the factor of three larger time step that could be used by the variable-order approximation. The variable-order approximation used lower-order approximations in the smaller elements found in the neighborhood of the airfoil, thus permitting a larger time step.

Next, we present results for the $k_1 = k_2 = 1$ case. The rms surface pressure is shown in Fig. 8. The acoustic intensity at 4.0 chord lengths is shown in Fig. 9. In Figs. 8 and 9, we show solutions computed using the gust amplitude of $\epsilon = 0.02$ and an amplitude of $\epsilon = 0.002$ scaled to the amplitude of the first. Also included in Figs. 8 and 9 is the solution from the GUST3D code.[22] There is a significant difference between the GUST3D solution and the solutions computed here. Note that the GUST3D solution does not show

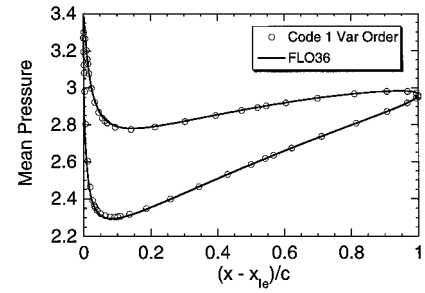

Fig. 10 Steady surface pressure for the lifting airfoil as a function of distance along the horizontal, scaled to the chord length.

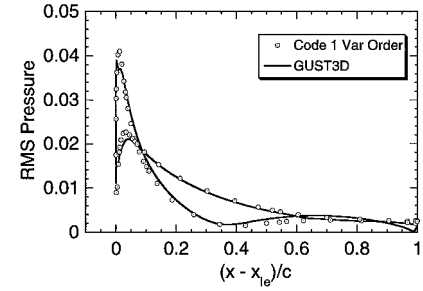

Fig. 11 Lifting airfoil with gust wave number $k = 1$ rms surface pressure.

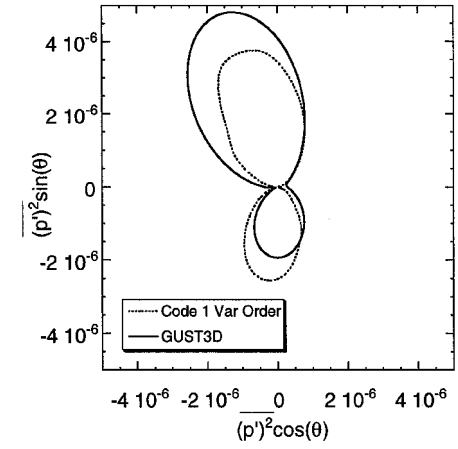

Fig. 12 Acoustic intensity at radius eight for the lifting airfoil with gust wave number $k = 1$.

backscatter in the upstream direction, corresponding to $\theta = 180$ deg, even though the leading edge is blunt, whereas the current computations do; compare Fig. 7. That the nonlinear computations at the two gust amplitudes match indicates that the intensity differences are not due to nonlinear effects.

C. Lifting Airfoil Solutions

Finally, we present solutions to the lifting airfoil case for wave number $k_1 = k_2 = 1$. Figures 10–12 show the results compared to the reference solutions. As earlier, the mean and rms pressures along the airfoil surface are in good agreement with the GUST3D solutions. Again, there are significant differences in the acoustic intensity at a radius of 4.0 chord lengths. The current computations show a small backscatter in the upstream direction, $\theta = 180$ deg, that is not seen in the GUST3D solutions. In the downstream direction, $\theta = 0$ deg, the current computations indicate a node where GUST3D does not.

IV. Conclusions

In this paper, we have used two discontinuous spectral element codes to compute the acoustic response of a flat plate and two airfoils to a vortical gust. Practical features of the method are the ability to vary the mesh size and approximation order to resolve local solution

features. The method is compact and robust and does not need the addition of artificial damping in the presence of sharp edges.

The flat plate solutions were compared to semi-analytic solutions. Computed solutions were within 1% of the analytic solution for $k_1 = k_2 = 1$ and 2% for $k_1 = k_2 = 3$.

The finite thickness airfoil solutions were computed for $k = 3$ and 1 for the nonlifting airfoil, and for $k = 1$ for the lifting case. Solutions using different meshes and damping layers were consistent with each other, as shown in the $k = 3$ nonlifting case. Surface quantities were in good agreement with the GUST3D solutions for both airfoils at $k = 1$. The intensities at 4.0 chord lengths, however, differ significantly from the reference solution. This difference cannot be accounted for by nonlinear effects.

Acknowledgments

This work was supported in part by NASA through Grant NAG-1-1889. The authors would like to thank James Scott for providing his reference solutions, including the FLO36, semianalytic, and GUST3D solutions, for comparison.

References

[1]Hariharan, S., Yu, P., and Scott, J., "Time Domain Numerical Calculations of Unsteady Vortical Flows About a Flat Plate Airfoil," *Journal of Computational Physics*, Vol. 101, No. 2, 1992, pp. 419–430.

[2]Grace, S., Hariharan, S., and Atassi, H., "Direct Computations of Unsteady Flows About Thin Airfoils," *Journal of Computational Acoustics*, Vol. 6, No. 2, 1998, pp. 337–355.

[3]Lockard, D. P., and Morris, P. J., "Radiated Noise from Airfoils in Realistic Mean Flows," *AIAA Journal*, Vol. 36, No. 6, 1998, pp. 907–914.

[4]Lockard, D., and Morris, P., "A Parallel Implementation of a Computational Aeroacoustic Algorithm for Airfoils Noise," *Journal of Computational Acoustics*, Vol. 5, No. 4, 1997, pp. 337–353.

[5]Hariharan, S., Scott, J., and Kreider, K., "A Potential Theoretic Method for Far Field Sound Calculations," *Journal of Computational Physics*, Vol. 164, No. 1, 2000, pp. 143–164.

[6]Canuto, C., Hussaini, M., Quarteroni, A., and Zang, T., *Spectral Methods in Fluid Dynamics*, Springer-Verlag, New York, 1987, Chap. 13.

[7]Black, K., "A Conservative Spectral Element Method for the Approximation of Compressible Fluid Flow," *Kybernetika*, Vol. 35, No. 1, 1999, pp. 133–146.

[8]Kopriva, D., "Euler Computations on Unstructured Quadrilateral Grids by a Staggered-Grid Chebyshev Method," AIAA Paper 98-0132, 1998.

[9]Tam, C., and Kurbatskii, K., "Microfluid Dynamics and Acoustics of Resonant Liners," *AIAA Journal*, Vol. 38, No. 8, 2000, pp. 1331–1339.

[10]Kopriva, D. A., and Kolias, J. H., "Solution of Acoustic Workshop Problems by a Spectral Multi-Domain Method," *ICASE/LARC Workshop on Benchmark Problems in Computational Aeroacoustics (CAA)*, NASA CP-3300, 1995, pp. 117–124.

[11]Bismuti, P., and Kopriva, D., "Solution of Acoustic Scattering Problems by a Staggered-Grid Spectral Domain Decomposition Method," *Second Computational Aeroacoustics (CAA) Workshop on Benchmark Problems*, NASA CP-3352, 1997, pp. 69–78.

[12]Stanescu, D., Kopriva, D., and Hussaini, M., "Dispersion Analysis for Discontinuous Spectral Element Methods," *Journal of Scientific Computing*, Vol. 15, No. 2, 2001, pp. 149–171.

[13]Hu, F. Q., Hussaini, M., and Rasetarinera, P., "An Analysis of the Discontinuous Galerkin Method for Wave Propagation Problems," *Journal of Computational Physics*, Vol. 151, No. 2, 1999, pp. 921–946.

[14]Rasetarinera, P., Hussaini, M., and Hu, F. Q., "Some Remarks on the Accuracy of the Discontinuous Galerkin Method," *Proceedings of the International Symposium on Discontinuous Galerkin Methods*, edited by B. Cockburn, G. Karniadalkis, and C.-W. Shu, Springer-Verlag, New York, 1999, pp. 407–412.

[15]Kopriva, D. A., and Kolias, J. H., "A Conservative Staggered-Grid Chebyshev Multidomain Method for Compressible Flows," *Journal of Computational Physics*, Vol. 125, No. 1, 1996, pp. 244–261.

[16]Patera, A., "A Spectral Element Method for Fluid Dynamics—Laminar Flow in a Channel Expansion," *Journal of Computational Physics*, Vol. 54, No. 3, 1984, pp. 468–488.

[17]Roe, P., "Approximate Riemann Solvers, Parameter Vectors, and Difference Schemes," *Journal of Computational Physics*, Vol. 135, No. 2, 1997, pp. 250–258.

[18]Kopriva, D. A., "A Conservative Staggered-Grid Chebyshev Multidomain Method for Compressible Flows. II. A Semi-Structured Method," *Journal of Computational Physics*, Vol. 128, No. 2, 1996, pp. 475–488.

[19]Stanescu, D., Ait-Ali-Yahia, D., Habashi, W. G., and Robichaud, M. P., "Multidomain Spectral Computations of Sound Radiation from Ducted Fans," *AIAA Journal*, Vol. 37, No. 6, 1999, pp. 296–302.

[20]Atassi, H., Dusey, M., and Davis, C., "Acoustic Radiation from a Thin Airfoil in Nonuinform Subsonic Flows," *AIAA Journal*, Vol. 31, No. 1, 1993, pp. 12–19.

[21]Jameson, A., "A Multi-Grid Scheme for Transonic Potential Calculations on Arbitrary Grids," *Proceedings of the 4th AIAA Computational Fluid Dynamics Conference*, AIAA, New York, 1979, pp. 122–146.

[22]Scott, J., and Atassi, H., "A Finite-Difference, Frequency-Domain Numerical Scheme for the Solution of the Gust Response Problem," *Journal of Computational Physics*, Vol. 119, No. 1, 1995, pp. 75–93.

P. J. Morris
Associate Editor